Journal of Solid State Chemistry, accepted September 2001

An integrated surface science approach towards metal oxide catalysis

Werner Weiss* and Robert Schlögl

Fritz-Haber-Institut der Max-Planck-Gesellschaft, Faradayweg 4-6, 14195 Berlin, Germany.

*Corresponding author

Abstract:
The function of a metal oxide catalyst was investigated by an integrated approach, combining a variety of surface science techniques in ultrahigh vacuum with batch reactor conversion measurements at high gas pressures. Epitaxial FeO(111), Fe_3O_4(111) and α-Fe_2O_3(0001) films with defined atomic surface structures were used as model catalysts for the dehydrogenation of ethylbenzene to styrene, a practized selective oxidation reaction performed over iron oxide based catalysts in the presence of steam. Ethylbenzene and styrene adsorb onto regular terrace sites with their phenyl rings oriented parallel to the surface, where the π-electron systems interact with Lewis acidic iron sites exposed on Fe_3O_4(111) and α-Fe_2O_3(0001). The reactant adsorption energies observed on these films correlate with their catalytic activities at high pressures, which indicates that the surface chemical properties do not change significantly across the pressure gap. Atomic defects were identified as catalytically active sites. Based on the surface spectroscopy results a new mechanism was proposed for the ethylbenzene dehydrogenation, where the upward tilted ethylgroup of flat adsorbed ethylbenzene is dehydrogenated at Brønsted basic oxygen sites located at defects and the coupling of the phenyl ring to Fe^{3+} terrace sites determines the reactant adsorption-desorption kinetics. The findings are compared to kinetic measurements over polycrystalline catalyst samples, and an extrapolation of the reaction mechanism found on the model systems to technical catalysts operating under real conditions is discussed. The work demonstrates the applicability of the surface science approach also to complex oxide catalysts with implications for real catalysts, provided suitable model systems are available.

1. Introduction

Metal oxide catalysts are used for many important synthesis reactions in chemical industry, but often the mode of operation of oxide catalysts is not well understood on an atomic scale. Our basic knowledge on metal oxide surface chemistry greatly lacks behind to those of metals, and not much is known yet about fundamental relationships between the catalytic function of oxide materials and their chemical compositions, crystallographic structures and electronic properties at the surface. This knowledge is needed for an effective targeted catalyst development strategy for complex oxide catalysts.
Modern surface science techniques allow to characterize surface structures and chemical compositions of small area single crystal samples, which can be used as model systems for studying heterogeneous catalytic reactions on a molecular level. Over the last 30 years such studies have revealed a detailed understanding of chemisorption and activation of molecules on metals [1]. Trends of catalytic activities of metals across the periodic table can be explained by their electronic structures at the surface [2,3], and adsorption properties of bimetallic surface alloys [4] and surface defects are mostly understood [5,6]. For many reactions the pressure gap could be bridged in a first step by combining surface science studies on single crystal samples with kinetic measurements at elevated gas pressures [7], and in some cases the turnover numbers on single crystal samples agreed with those of high area supported metal catalyst samples [8,9]. In case of the ammonia synthesis reaction detailed nitrogen chemisorption studies over iron single crystals revealed the dissociative chemisorption of N_2 as the rate determining step and the parameters for a microkinetic model [10], which was able to correctly extrapolate the catalyst performance to technical reaction conditions [11]. Comparative experiments over polycrystalline catalyst samples substantiated the model study results and contributed to bridge the "material gap" between single crystals and polycrystals [12-14]. In addition to strong recent efforts for studying reactions on small metal particles deposited onto oxide supports [15], molecular surface characterization techniques operating under high pressure reaction conditions were developed like for example scanning tunneling microscopy (STM) [16,17], sum frequency generation (SFG) [18] and near edge x-ray absorption spectroscopy (NEXAFS) [19-21]. These techniques represent a major progress in bridging the pressure-gap, since they allow to directly study structural changes on the model catalyst surfaces induced by the high pressure gaseous environment as well as the dynamics of such restructuring processes. However, one should be aware that the data can only be interpreted on the basis of knowledge accumulated from classical surface science experiments during the last 35 years.
Selective oxidation reactions performed on metallic and semiconducting oxide catalysts are a combination of redox and acid-base reactions. The influence of acidic and basic surface sites on the activity of metal oxide catalysts was studied in numerous investigations over polycrystalline samples, but still not much is known about the detailed nature of active sites. A direct elucidation of catalytically active sites requires model systems with ordered and defined surface structures, including surface defects deviating from ideally terminated surfaces, which might play an important role within this context. Comparative studies on such samples with different orientations or stoichiometries can provide fundamental insight into the role of acidic

and basic surface sites, the oxide electronic structure, and the geometric surface structure for the catalytic activity of oxide materials. The preparation of suitable model systems for such studies is a challenging task and represents the key problem within this field of research. From a large number of surface science studies performed on single crystal metal oxide samples it turned out that the preparation of ordered metal oxide surfaces with defined structures and compositions is very difficult [22-24]. In addition to cleanliness and surface order a defined surface stoichiometry must be established. Since the stoichiometry of binary oxides is thermodynamically controlled by temperature and oxygen pressure [25], some oxide phases must be prepared at high pressures. They can be stabilized in ultrahigh vacuum by kinetic hindering after cooling down the sample from the elevated preparation temperature inside the high pressure environment. Also, the experimental or theoretical determination of metal oxide surface structures is difficult, because oxide crystal structures often are complex and several different surface terminations have to be taken into account in a structure analysis, in particular in case of polar surface planes.

Using single crystal bulk samples experimental problems like electrostatic charging in case of insulating oxides are encoutered when appling electron spectroscopy or STM. High pressure reaction experiments over single crystal samples are problematic and were never done so far, as it might be very difficult to clean and restore the initial surface of such samples after such experiments. Most of these problems can be circumvented by using thin epitaxial oxide films grown onto conducting metal substrates. Well ordered thin of several transition metal oxides [26,27]were prepared by oxidizing the surface regions of the corresponding metal single crystal samples, and thin films of alumina were obtained by oxidizing the sirface of NiAl alloy single crystals [28]. Heteroepitaxial growth of metal oxide films onto dissimilar metal single crystal substrates is another technique, which was done successfully for a large number of oxide overlayer–substrate systems [29-35]. When using chemically inert substrates this technique allows to prepare different transition metal oxide phases with defined stoichiometries by choosing the proper preparation conditions, since no oxygen can diffuse into the substrate in an uncontrolled manner. High pressure reaction studies can be performed more easily on thin epitaxial films, since if contaminated they can be removed from the substrate and a fresh surface can be prepared.

This paper describes an integrated surface science approach tackling the styrene synthesis reaction, a selective oxidation where ethylbenzene is dehydrogenated to styrene over potassium promoted iron oxide catalysts in the presence of steam. So far one model system study of this reaction was performed by Goodman et al., who prepared iron oxide films by oxidizing the surface region of a polycrystalline iron sample [36]. In order to obtain model systems with ordered and defined atomic surface structures we grow thin epitaxial FeO(111), Fe_3O_4(111), and α-Fe_2O_3(0001) model catalyst films onto Pt(111) substrates. Their surface structures and surface defect concentrations were determined with STM and low energy electron diffraction (LEED) crystallography, their electronic structures and surface compositions by photoelectron spectroscopy (UPS, XPS) and NEXAFS. The adsorption of H_2O, EB and St onto these films was investigated by TDS, XPS, UPS and NEXAFS. These comparative studies provided fundamental insight into the role of the surface termination and electronic structure for the adsorption properties of iron oxides and metal oxides in general. The reactant adsorption-desorption elementary step kinetics on Fe_3O_4(111) and α-Fe_2O_3(0001) observed with TDS agree with the catalytic activities of these two oxide phases observed at high gas pressures, which indicates that the surface chemical properties of the model catalyst films do not change singnificantly across the pressure-gap. Based on the surface science experimental results a reaction mechanism was proposed for the ethylbenzene dehydrogenation [37], and the possibility to extrapole this mechanism to technical iron oxide catalysts operating beyond the pressure-material gap is discussed.

2. The conversion of ethylbenzene to styrene

The reaction

$$C_6H_5CH_2CH_3 \rightarrow C_6H_5CHCH_2 + H_2 \qquad (1)$$

is an endothermic dehydrogenation as no oxidant is used in the process (ΔH=129.4 kJ/mol). It is performed at temperatures around 900 K in excess of steam. The main side products of the process are benzene and toluene. Since 1957 the industrial catalyst is principally a potassium-promoted iron oxide although a variety of other oxides are added in small concentrations [38]. Today 15 million tons product per year are produced, which makes even small improvements of the catalyst profitable. An extensive review on the development of the styrene synthesis catalyst was published by Lee in 1973 [39], a recent review can be found in reference [40]. Kinetic studies of the EB dehydrogenation were performed over polycrystalline catalyst samples by a number of authors [41-45]. A unimolecular Langmuir-Hinshelwood mechanism was proposed, where the reaction rate depends on the adsorption-desorption equilibrium of EB and styrene. Potassium increases the activity of pure iron oxide catalysts by one order of magnitude, although very similar apparent activation energies were obtained for promoted and unpromoted catalysts. This indicates the existence of active sites with identical properties on promoted and unpromoted catalyst surfaces, where potassium just increases the number of active sites. First the catalyst function was explained by a strong Brønsted base consisting of liquid KOH supported on porous iron oxide [46], a model that was dismissed lateron. Hirano first proposed an active $KFeO_2$ phase on the catalyst surface, based on X-ray diffraction measurements on spent and ”steamed” catalysts in the absence of air [44]. This was substantiated later by Muhler et al., who performed a multi-method study devoted to the structure of the active phase of technical iron oxide catalysts [47-48]. There, the formation of an active $KFeO_2$ surface phase was observed under reaction conditions, and the activity of the catalyst was found to scale with the surface abundance of $KFeO_2$. Similar speculative acid-base bifunctional reaction mechanisms were proposed for the dehydrogenation of ethylbenzene over iron oxide catalysts [49], over binary oxides containing TiO_2 [50] and over oxygen containing organic polymers [51]. They all assume a combined acid-base redox reaction, where ethylbenzene adsorbs via two C-H groups of the ethylgroup onto neighboring acidic metal and basic oxygen sites or onto two Brønsted basic oxygen sites. These sites deprotonate the two C-H groups of the ethyl group and simultaneously two electrons are transferred to the catalyst, which reduce two Fe^{3+} species to Fe^{2+} in case of the iron oxide catalyst. This results in styrene, two hydroxyl groups on the catalyst surface and two reduced Fe^{2+} species. The catalytic cycle gets completed by desorption of hydrogen and reoxidation of Fe^{2+} to Fe^{3+}.

Steam acts as a diluent and is assumed not to take part in the reaction mechanism. It supplies heat needed for running the endothermic reaction and shifts the equilibrium to the product side thereby enhancing the styrene conversion. Furthermore, it reacts with carbonaceous surface deposits to CO and CO_2 and prevents a reversible deactivation of the catalyst by coke. In technical flow reactor systems short contact times have to be established in order to prevent the formation of carbonaceous deposits and the polymerization of styrene [40]. The deactivation and regeneration by steam has been studied in detail in flow reactor sytems as well as in the context of multifunctional reactor concepts [52,53]. The model system investigations of the styrene synthesis reaction performed by Goodman et al., where catalytic activities of polycrystalline iron oxide films characterized by surface science techniques in UHV were studied in high pressure batch reactor experiments, mainly confirmed previous findings on this reaction system [36].

3. Experimental approach and model catalyst preparation

The experiments were done in the three chamber UHV surface analysis system depicted in Fig. 1 [54]. All three chambers are equipped with standard sample cleaning facilities, iron evaporators and backview LEED optics. The central TDS and STM chambers are further equipped with AES spectrometers and high pressure cells that can be completely separated from the analysis chambers by gate valves. They are used for preparing oxide films by high pressure oxidation treatments and they contain the batch reactor system employed in these studies. The platinum single crystal substrates have a diameter of 1 cm and are mounted onto sample holders fabricated from single crystalline sapphire, which provide good thermal contact so that the samples can be cooled to liquid nitrogen temperature when placed onto the manipulators. Sample heating on the UHV manipulators is performed by electron bombardment from the back, in the high pressure cells resistive heating is performed as descibed in detail in ref. [54]. The samples can be transferred into the different chambers and into the separate high pressure cells by the magnetic rods visible in Fig. 1, while on every sample station spring electric feedthrough contacts provide thermocouple temperature control. Thus, STM, TDS and high pressure batch reactor measurements can be peformed on the same sample at precise temperatures. This represents the key requirement of the experimental approach applied here, since it allows to determine adsorption-desorption elementary step kinetics by TDS and to measure catalytic activities by high pressure batch reactor measurements on the same sample. The photoelectron spectroscopy experiments were done in a separate chamber equipped with the same sample transfer system and a high pressure cell [55]. NEXAFS measurements were done in similar UHV chambers utilizing synchrotron radiation from the storage ring BESSY I in Berlin [56].
Fig. 2 depicts the preparation procedure of epitaxial iron oxide model catalyst films. Onto a clean Pt(111) surface monolayer amounts of iron are deposited at room temperature and subsequently oxidized for 2 min in 10^{-6} mbar oxygen at temperatures between 870 and 1000 K. This creates well ordered FeO(111) films 1-2 monolayer thick, which completely wet the substrate surface. After numerous iron deposition-oxidation cycles 100-200 Å thick Fe_3O_4(111) films are obtained, which are transformed into α-Fe_2O_3(0001) films by a high pressure oxidation treatment in 1 mbar oxygen at 1100 K for about 10 min, a phase transformation that is expected from the bulk phase diagram of the iron-oxygen system [57]. After the oxidation procedure the α-Fe_2O_3(0001) films are cooled down to room temperature in the high pressure environment, then the oxygen is pumped off and the samples are transfered from the high pressure cell back into the UHV analysis chambers where they remain stable. All three iron oxide phases form well ordered surface structures descibed in the next section. Because the platinum substrate is inert against oxidation under the conditions applied here, the heteroepitaxial growth allows to control the oxide film stoichiometry by choosing different oxygen partial pressures and oxidation temperatures as described above. This would not be possible when using bulk single crystal samples or when preparing thin films by oxidizing the surface region of an iron single crystal sample, because of uncontrolled oxygen diffusion from the surface into the substrates or vice versa. The iron oxide films are thermally stable up to temperatures around 1100 K when they start to desorb from the Pt(111) substrate.

4. Geometric and electronic surface structures of epitaxial iron oxide films

Fig. 3 shows atomic resolution STM images of the three iron oxide films grown onto Pt(111) (top), the corresponding LEED patterns (middle) and surface structure models in top view representations (bottom). The STM image of the first FeO(111) layer exhibits a hexagonal lattice of protrusions with a 3.1 Å periodicity and a moiré superstructure with a 25 Å periodicity. This film was prepared for the first time by Vurens et al. [58]. Electron-scattering quantum-chemistry theory calculations simulating this STM image revealed the atomic protrusions to occur at oxygen atom positions located in the topmost layer of this film [59]. The model consists of a close-packed iron-oxygen (111) bilayer with oxygen located on top, which was confirmed by photoelectron diffraction measurements [60]. The film is laterally slightly expanded and the iron-oxygen interlayer distance is reduced when compared to bulk FeO. The moiré superstructure in the STM image and the characteristic satellite spots in the LEED pattern are caused by the 12% lattice mismatch to the substrate [61]. The first bilayer completeley wets the platinum substrate, and depending on the exact oxidation temperature second and third bilayers grow in a layer-by-layer mode. They form the same oxygen terminated surface structures and slightly different interlayer relaxations [62].
Upon formation of 1-2 ML thick FeO(111) films a three-dimensional growth of Fe_3O_4(111) islands begins, resulting in a Stranski-Krastanov growth mode for iron oxides on Pt(111) [63]. These islands eventually coalesce and form closed Fe_3O_4(111) films at least 100 Å thick, which consist of hexagonally shaped crystallites with lateral dimensions around 1000 Å. They expose atomically flat terraces separated by monoatomic steps 4.8 Å high, which occur with average distances around 300 Å. The vertical roughness ranges between 30 and 100 Å on a length scale of 1 μm, which compares to typical surface morphologies on single crystal samples. One single surface termination is formed after a final oxidation treatment at 1000 K [64]. It exhibits a hexagonal lattice of protrusions with a 6 Å periodicity in the atomic resolution STM image in Fig.3, as well as randomly distributed missing protrusions. The 6 Å periodicity also corresponds to the LEED pattern observed for this film. Fe_3O_4 magnetite crystallizes in the cubic inverse spinel structure, where the oxygen anions form a close-packed fcc

sublattice with tetrahedrally and octahedrally coordinated Fe^{2+} and Fe^{3+} cations located in interstitial sites [65]. The $Fe_3O_4(111)$ surface structure was determined by a full dynamical LEED intensity analysis and is displayed in the top view model depicted in Fig. 3 [66]. It exposes ¼ monolayer of iron cations located over a close-packed oxygen layer underneath. The first four interlayer spacings are strongly relaxed, which is characteristic for polar surface terminations of ionic compound materials. Based on this result we assign the protrusions in the atomic resolution STM image to the topmost layer iron cation positions. This interpretation is supported by ab-initio calculations performed for the relaxed $Fe_3O_4(111)$ surface, which revealed a high density of occupied and unoccupied Fe3d states located close above and below the Fermi level, which are related to the topmost iron atoms [64]. The missing protrusions in the STM image represent the most abundant type of point defects and are attributed to surface iron vacancies.

The $Fe_3O_4(111)$ films can be transformed into α-$Fe_2O_3(0001)$ films by a high pressure oxidation treatment. α-Fe_2O_3 hematite crystallizes in the corundum structure, where the oxygen anions form an hcp sublattice with octahedrally coordinated Fe^{3+} cations located in interstitial sites [67]. As predicted by recent ab-initio calculations performed for the α-$Fe_2O_3(0001)$ surface [68], we observe the formation of a purely oxygen terminated α-$Fe_2O_3(0001)$ surface structure in oxygen pressures of 1 mbar, whereas an iron-terminated surface is formed in 10^{-5} mbar oxygen [69]. The STM image of the iron terminated surface in Fig. 3 exhibits a hexagonal lattice of protrusions with a 5 Å periodicity, which corresponds to the LEED pattern of this film. Mostly monoatomic steps 2.3 Å high are observed. Fig. 3 shows a top view model of this the iron terminated α-$Fe_2O_3(0001)$ surface structure structure, which was determined recently by a dynamical LEED intensity analysis [70]. Like on $Fe_3O_4(111)$ strong interlayer relaxations were found in the surface region, as predicted by the ab-initio calculations. Again, the protrusions in the STM image are assigned to the topmost iron atom positions on this surface, which is supported by the calculations that reveal a high density of unoccupied Fe3d states located close above the Fermi level.

Both occupied and unoccupied electronic states of the iron oxide films were investigated using photoelectron spectroscopy (XPS, UPS) and NEXAFS [71-73]. All data obtained from the $Fe_3O_4(111)$ and α-$Fe_2O_3(0001)$ multilayers agree well with data from polycrystalline and single crystal bulk samples, which demonstrates that the films are equivalent to their bulk oxide counterparts. The valence and conduction bands in iron oxides are made up of Fe3d states hybridized with O2p states, leading to iron-oxygen bonds with mixed covalent and ionic character. Both oxides form high spin configurations, which results in ferrimagnetic and anti-ferromagnetic states for Fe_3O_4 and α-Fe_2O_3, respectively [74]. Fe_3O_4 is a metallic oxide containing a metallic minority spin-down band that crosses the Fermi level and a semiconducting majority spin-up band forming a bandgap [75]. In a localized picture the metallic character can be attributed to electron hopping from Fe^{2+} to Fe^{3+} cations located in octahedral interstitials, where the cation charges 2+ and 3+ always have to be considered as formal charges which are higher than the real cation charges because of the covalent bonding character. α-Fe_2O_3 is a charge transfer insulator with a band gap of 2 eV [76]. In both oxides the highest occupied and lowest unoccupied states near the Fermi level are mainly of Fe3d character, whereas O2p states start to dominate 5-6 eV below and above the Fermi level [77,78]. On the $Fe_3O_4(111)$ films a $3d^6L$ (L is an oxygen ligand) final state related to Fe^{2+} species shows up in the valence band spectra about 1 eV below the Fermi level, whereas no Fe^{2+} species are detected on the α-$Fe_2O_3(0001)$ films using highly surface sensitive photon energies. This indicates only Fe^{3+} species to exist on the iron terminated α-$Fe_2O_3(0001)$ surface, and Fe^{2+} possibly coexisting with Fe^{3+} species on $Fe_3O_4(111)$. In the FeO(111) films only Fe^{2+} species are detected with XPS, indicating an ionic Fe-O bonding character also in these thin films. However, the UPS and NEXAFS data differ somewhat from those of FeO bulk samples, indicating a different electronic structure if compared to bulk FeO which may be caused by the two dimensional character of these films and by coupling to substrate Pt5d states.

5. Reactant chemisorption by interaction with acidic surface metal sites

5.1 Dissociative adsorption of water

We studied the adsorption of water since the styrene synthesis reaction is performed in excess of steam, and because water acts as a probe molecule that can reveal information about acidic and basic surface adsorption sites. Since the styrene synthesis reactant atmosphere represents a slightly reducing environment with no oxygen present, an iron terminated α-$Fe_2O_3(0001)$ surface is expected to form under these conditions and thus has been prepared for all adsorption and catalytic activity studies presented in the following.

Fig. 4a shows TDS traces of water adsorbed onto FeO(111), $Fe_3O_4(111)$ and α-$Fe_2O_3(0001)$. On FeO(111) weakly bound water species labeled β desorb with first order kinetics at temperatures around 170 K. Fig. 4b shows the UPS valence band difference spectrum of this adsorbate species, which is characteristic for molecular water with emission from the three highest occupied water orbitals $1b_1$, $3a_1$ and $1b_2$. The three molecular orbitals are shifted by a relaxation shift of 1.8 eV towards lower binding energies due to substrate induced final state screening, but their relative binding energy separations are identical to those of gaseous water [79]. Thus, water monomers physisorb onto FeO(111) without chemical interaction to the substrate. As the coverage increases a hydrogen bonded water bilayer is formed, followed by the condensation of hydrogen bonded ice multilayers desorbing with zero order kinetics at temperatures around 160 K (labeled α in Fig. 4a).

On $Fe_3O_4(111)$ and α-$Fe_2O_3(0001)$ the TDS traces show a desorption signal around 280 K labeled γ. It corresponds to dissociatively adsorbed water as concluded from the valence band difference spectrum of water on $Fe_3O_4(111)$ shown in Fig. 4b, where only two maxima corresponding to emission from 3σ and 1π molecular orbitals of adsorbed hydroxyl groups can be seen. Calibrated TDS and XPS measurements revealed a hydroxyl saturation coverage that corresponds to about one hydroxyl group per Fe site exposed on this surface, which is much higher than surface defect concentrations observed with STM [80]. Thus, the dissociation is not related to defects but predominantly takes place on regular surface areas of the

$Fe_3O_4(111)$ films. As can be seen in the TDS spectra in Fig. 4a, after saturation of dissociatively adsorbed water molecular water species labeled β get coadsorbed followed by the condensation of ice multilayers labeled α.
On FeO(111) exposing an outermost close-packed oxygen layer water is physisorbed without chemical interactions, whereas a dissociative adsorption resulting in adsorbed hydroxyl species takes place on the defect free $Fe_3O_4(111)$ surface exposing ¼ ML of Fe atoms located above a close-packed oxygen layer. This comparison proves that the dissociation occurs via interaction with Fe sites exposed on $Fe_3O_4(111)$, which are absent on the inert FeO(111) surface. A likely reaction scheme is depicted in Fig. 4c [81]. The water molecule gets associatively adsorbed with the Lewis basic oxygen lone pair orbital onto an Lewis acidic surface Fe site, and a substrate-adsorbate bond gets established by interaction between the water HOMO $1b_1$ orbital and empty Fe3d orbitals energetically located in the lower conduction band region. This weakens an OH bond within the water molecule and leads to dissociation. The resulting OH^- group remains adsorbed at the Fe site and the H^+ species is adsorbed onto a neighboring O site, as depicted in Fig. 4c. The heterolytic dissociation of water is an acid-base reaction, which can proceed very effectively on $Fe_3O_4(111)$ because Lewis acidic Fe cations and neighboring Brønsted basic O anions are located in a distance that fits to the geometry of the water molecule quite well. Since very similar TDS spectra are observed for water adsorbed onto the iron terminated α-$Fe_2O_3(0001)$ surface, a dissociative adsorption seems to occur on this oxide phase, too.
The water dissociation is a non-activated process with an adsorption enthalpy of about 65 kJ/mol, a value similar to those observed on many polycrystalline oxide samples [82]. For water physisorbed on FeO(111) a rather similar adsorption enthalpy of 52 kJ/mol is obtained. Despite these similar values large coverage differences are observed under adsorption-desorption equilibrium conditions. At a vapor pressure of $p_{H2O}=10^{-6}$ mbar a saturated hydroxyl layer is formed on $Fe_3O_4(111)$ at 300 K whereas no water is physisorbed on FeO(111) at temperatures above 180 K [80]. This is due to the slow recombinative desorption of OH^- and H^+ species, which takes place with a second order frequency factor of $2.4\times10^{-6}cm^2s^{-1}$ and which is caused by a high mobility of the H^+ species as directly observed with STM [83].

5.2. Molecular chemisorption of ethylbenzene and styrene

Similar to water also ethylbenzene (EB) and styrene (St) interact very different with oxygen and iron terminated iron oxide surfaces [55, 84, 85]. Fig. 5a shows TDS traces obtained after exposing FeO(111), $Fe_3O_4(111)$ and α-$Fe_2O_3(0001)$ surfaces to small amounts of EB and St, when only the most strongly bound adsorption states are populated. With increasing exposures new desorption maxima appear at lower temperatures due to physisorbed β and condensed α species (not shown here), similar to the water TDS spectra in Fig. 4a. On FeO(111) St desorbs at a slightly higher temperature (210 K) than EB (220 K), both species desorb with first order kinetics. The corresponding desorption energies are around 55 kJ/mol, indicating weak interactions. Fig.5b shows the UPS valence band difference spectrum of the EB adsorbed on FeO(111). It is identical to spectrum of condensed EB multilayers, which compare well with EB gas-phase spectra after a relaxation shift of $E_R=2.3$ eV to lower binding energies. The same is observed for St adsorbed on FeO(111) (not shown here). Thus, the electronic structures of EB and St do not change upon adsorption onto the oxygen terminated FeO(111) surface, indicating physisorption without chemical interaction to the substrate.
On the iron terminated $Fe_3O_4(111)$ and α-$Fe_2O_3(0001)$ surfaces a first order desorption of EB and St occurs at considerably higher temperatures, resulting in desorption energies of 86 kJ/mol (118 kJ/mol) for EB (St) on $Fe_3O_4(111)$ and 64 kJ/mol (73 kJ/mol) for the dominating EB (St) signals labeled γ_1 on α-$Fe_2O_3(0001)$. Fig. 5b shows the valence band difference spectrum of EB adsorbed on $Fe_3O_4(111)$. It still looks similar to the EB condensate spectrum with only a slightly smaller relaxation shift of 1.9 eV, indicating a non-dissociative chemisorption of EB. However, the HOMO π-orbital is shifted by 0.4 eV towards higher binding energy and a shoulder at the low binding energy side can be seen. Like for the dissociative adsorption of water the saturation coverages of the chemisorbed EB and St species are high and indicate adsorption on regular surface areas. The amount of chemisorbed species decreases as the surface defect concentrations increases, and no additional adsorption states with higher binding energies appear on highly defective films. Thus, no specific chemisorption at defects exists, and adsorption sites located near defects must have the same adsorption energies as adsorption sites located on terraces far away from defects. A work function decrease indicates a polarization of chemisorbed EB molecules with negative charge shifted towards the substrate. Similar results are observed for styrene. Thus, EB and St chemisorb molecularly on $Fe_3O_4(111)$ and α-$Fe_2O_3(0001)$ via specific interactions of their π-electron systems with exposed surface iron atoms, whereas no chemical interaction takes place on the purely oxygen terminated FeO(111) surface.
The orientations of the chemisorbed EB and St molecules were determined by NEXAFS [56]. Fig. 5c shows carbon K-edge absorption spectra of submonolayer amounts of EB and St chemisorbed on $Fe_3O_4(111)$, measured under normal and grazing incidence of the incoming light with respect to the surface normal. On α-$Fe_2O_3(0001)$ similar spectra were obtained. The dominating resonance at 285 eV photon energy corresponds to a C1s → π* excitation into the lowest unoccupied molecular orbital (LUMO) of the phenyl ring, followed by resonances corresponding to excitations into higher lying π* and σ* orbitals. The resonances show strong dichroisms from which the tilt angle between the phenyl ring plane and the substrate surface can be calculated. For EB and St on $Fe_3O_4(111)$ and α-$Fe_2O_3(0001)$ we obtain flat adsorption geometries, where the phenyl ring is oriented parallel to the surface as depicted in Fig. 5d. A small broadening of the first π* resonance is observed, indicating a weak distortion of the LUMO orbitals upon chemisorption.
The spectroscopy results indicate a donor-acceptor interaction between chemisorbed EB or St and the iron-terminated iron oxide surfaces, as often the case in chemisorption systems. The adsorbate HOMO π-orbitals of the phenyl rings mix with unoccupied Fe3d states located in the lower conduction band regions of the substrates, which leads to stabilized bonding orbital combinations that shift the adsorbate HOMO orbitals to higher binding energies as observed by UPS for EB on $Fe_3O_4(111)$ (Fig. 5b). This interaction also can be considered as an acid-base reaction, where the Lewis basic EB and St species interact via their π-electron systems with Lewis acidic Fe^{2+}or Fe^{3+} surface sites. The interaction involves a negative charge transfer from the adsorbates to the substrates as indicated by the work function decrease. The Lewis acid-base picture explains the different chemisorption strenghts for EB and St on $Fe_3O_4(111)$ and α-$Fe_2O_3(0001)$ observed with TDS (Fig. 5a).

The highly polarizable soft Lewis bases EB and St interact strongly with the metallic $Fe_3O_4(111)$ surface exposing soft acidic Fe^{2+} sites, and their interaction becomes weaker with the semiconducting α-$Fe_2O_3(0001)$ surface exposing hard acidic Fe^{3+} sites. In general, the chemisorption strength of EB and St decreases with increasing Lewis acidity of the metal oxide surface. St always interacts stronger than EB because of the additional unsaturated C-C bond with a polarizable π-electron orbital.

5.3. Surface coverage extrapolation to styrene synthesis reaction conditions

From the TDS data presented above and from adsorption isobars measured with UPS the desorption energies ΔE_{des}, isosteric heats of adsorption $q_{st}=\Delta E_{des}-\Delta E_{ad}$ and preexponetial frequency factors ν_{des} for desorption were determined quantitatively [85]. Both for EB and St chemisorption is non-activated ($\Delta E_{ad} \approx 0$) with initial sticking coefficients s_0 close to unity. With these elementary step kinetic parameters microkinetic models can calculate catalytic conversions at high pressures and temperatures, assuming a reaction mechanism with one slowest rate determining step [86]. We performed a simple adsorbate coverage extrapolation to the styrene synthesis reaction conditions (T=873 K, $p_{EB}=p_{St}=100$ mbar) using the Langmuir formalism. The Langmuir formalism assumes that sticking occurs only on unoccupied sites without mobile precursor states. Although we observe a precursor adsorption kinetics at T=100 K, the lifetime and diffusion lenght of the precursor species become very small at the reaction temperature of T=900 K, so that one can assume a Langmuir adsorption kinetics at such high temperatures. The Langmuir isotherm gives the relative coverage Θ_r (number of occupied divided by the number of available adsorption sites) under adsorption-desorption equilibrium conditions [87]:

$$\Theta_r = bp/(1+b\,p) \qquad (2)$$

with p being the gas pressure and b given by

$$b = \{s_0/(\nu_{des}\, N\, (2\pi mkT)^{0.5})\}\, \exp\{-(\Delta E_{ad}-\Delta E_{des})/kT\}. \qquad (3)$$

Here, m is the mass of the adsorbing molecule, k the Boltzmann constant and T the temperature. The adsorption site density N on the model catalyst surfaces is estimated to be 2×10^{14} cm^{-2}. Considering the adsorption of only EB or St, we obtain relative coverages Θ_r for the chemisorbed species of EB (St) of 92 % (100%) on $Fe_3O_4(111)$ and 37% (29%) on α-$Fe_2O_3(0001)$ (majority species γ_1). The more strongly bound γ_2 minority species on α-$Fe_2O_3(0001)$ are always fully occupied and are neglected beause of their small number.

The chemisorption sites supposed to represent the catalytically active sites are populated almost completely on $Fe_3O_4(111)$ and by about 1/3 on α-$Fe_2O_3(0001)$. Coadsorption experiments revealed EB and St to chemisorb onto the same sites. Therefore, we can estimate the relative occupation of active sites by EB and by St produced from EB during the catalyst operation. We assume the conversion from EB to St to be fast and consider the competitive coadsorption of EB and St under equilibrium conditions, as given by the corresponding Langmuir isotherms:

$$\Theta_{r,EB} = b_{EB}\, p_{EB}/(1+b_{EB}\, p_{EB}+b_{St}\, p_{St}), \quad \Theta_{r,St} = b_{St}\, p_{St}/(1+b_{EB}\, p_{EB}+b_{St}\, p_{St}),$$

$$\text{and } \Theta_r = \Theta_{r,EB} + \Theta_{r,St}. \qquad (4)$$

Here, p_{EB} and p_{St} are the partial pressures of EB and St, which we assume to be 100 mbar each. Under these conditions we obtain for the total coverages $\Theta_r = \Theta_{r,EB} + \Theta_{r,ST}$ and relative coverage ratios Θ_{EB}/Θ_{ST} on $Fe_3O_4(111)$ Θ_r=100% and $\Theta_{EB}/\Theta_{ST}\approx0.004$, on α-$Fe_2O_3(0001)$ Θ_r=35% and $\Theta_{EB}/\Theta_{ST}\approx1.3$. On $Fe_3O_4(111)$ almost all chemisorption sites are blocked by the product molecule styrene, on α-$Fe_2O_3(0001)$ only 43% are blocked by styrene. This suggests no styrene conversion on $Fe_3O_4(111)$ because of site blocking and a possible styrene conversion on α-$Fe_2O_3(0001)$, provided the adsorption-desorption kinetics do not change significantly across the pressure-gap. This structure reactivity correlation is observed in the high pressure batch reactor experiments presented in the next section.

6. Model catalyst film activities at high gas pressures

The catalytic film activities were investigated in batch reactor experiments in a water-EB mixture with a molar ration of 10:1 and a total gas pressure of 0.6 mbar [88]. These conditions approximate the real situation of the technical styrene synthesis reaction. The batch reactor was located inside the high pressure cells and had a volume of about 1 ml. Reactor gas was leaked via a capillary into a mass spectrometer for product detection. On the left side of Fig. 6 the LEED patterns of three $Fe_2O_3(0001)$ films are shown before the reaction experiments were performed. As indicated the atomic surface defect concentrations on these films were quantified by the diffuse background intensities and diffraction spot widths in the LEED patterns, which increase with increasing step and point defect density, respectively [89,90].

Fig. 7a shows the results of the batch reactor experiments performed on the $Fe_2O_3(0001)$ films. H_2O and EB were admitted first, then the sample temperature was raised until the reaction temperature of 870 K was reached as indicated by the arrow. For the low defect density Fe_2O_3 film no significant changes in the EB and styrene signals are observed, indicating no catalytic styrene formation. Only a small increase of the hydrogen signal can be seen. On the medium and high defect density films stronger hydrogen and styrene formations are observed. With increasing surface defect concentrations an increasing formation of styrene and hydrogen is observed, accompanied by an increasing consumption of EB in the batch reactor. After about 30 min the active films were deactivated and the styrene and hydrogen product concentrations did not increase noticably with time anymore. Fig. 7b displays the reaction experiments performed on $Fe_3O_4(111)$ films with low and high surface defect concentrations. Independent on the surface defect concentrations no catalytic styrene formation is observed, no hydrogen evolution and no significant decrease of the EB concentration in the batch reactor.

After the reaction experiments the model catalyst films are covered with carbonaceous surface deposits. This is concluded from post reaction surface analysis by Auger electron spectroscopy, where graphitic carbon species are observed, as well as from the evolution of CO, CO_2 and H_2O during TPR experiments in the presence of oxygen. The hydrocarbon surface deposits can be seen in the PEEM images shown in Fig. 6. The clean iron oxide films exhibit dark PEEM images (not shown here). The inactive film with the lowest surface defect concentration is covered by small patches of carbon deposits, the dark areas inbetween reflect clean surface areas. Very similar PEEM images were observed on the inactive $Fe_3O_4(111)$ films, where carbon deposits have also formed. On the medium defect density film more deposits are visible in the PEEM image, and on the most active film a thick hydrocarbon layer has formed.
The reaction experiments revealed α-Fe_2O_3 as the active phase of the unpromoted iron oxide catalyst, whereas Fe_3O_4 is not active. The catalytic styrene formation on the α-$Fe_2O_3(0001)$ films increases with increasing surface defect concentration. This clearly reveals atomic surface defects as active sites for the dehydrogenation of EB to St over α-Fe_2O_3 catalysts. These defects can be atomic steps and/or point defects like adatoms or vacancies, which cannot be distinguished by our LEED measurements. During the batch reactor experiments hydrocarbon deposits are formed on the model catalyst films. They start to form at different surface regions, where mesoscopic structural defects might be located, and continue to grow from there resulting in larger patches on the surface. On the α-$Fe_2O_3(0001)$ films the growth of these carbonaceous deposits is correlated to the film activities and increases with increasing catalytic activity. After prolonged batch reactor operation the active Fe_2O_3 films are completely overgrown with deposits and deactivated for that reason.

7. Summary and conclusions

The chemisorption of all molecules investigated here (ethylbenzene, styrene and water) occurs via interaction with acidic iron atoms exposed on the defect free surfaces of $Fe_3O_4(111)$ and α-$Fe_2O_3(0001)$, whereas physisorption without chemical interaction takes place on the FeO(111) surface exposing no iron atoms. The heterolytic dissociation of water on $Fe_3O_4(111)$ can be considered as an acid-base reaction, which is facilitated by neighboring Lewis acidic iron and Brønsted basic oxygen sites. These sites are located on the surface in a distance that fits to the geometry of the water molecule, so that they can adsorb the resulting OH^- and H^+ species after activation and heterolytic dissociation of the molecule. EB and St chemisorb molecularly onto the same adsorption sites with their phenyl rings oriented parallel to the surface planes, where their HOMO π-electron orbitals couple to empty Fe3d orbitals of exposed iron sites. This interaction can also be considered as an acid-base reaction between the soft Lewis bases EB and St and Lewis acidic surface iron sites, where the chemisorption strength is related to the electronic structures or acid base characters of the reactant molecules and oxide surface sites. No defect related adsorption states with higher binding energies exist.
Assuming the adsorption-desorption elementary step kinetic parameters not to change significantly across the pressure-gap, a Langmuir extrapolation to the technical styrene synthesis reaction conditions reveals high coverages on $Fe_3O_4(111)$ with a complete site blocking by the styrene product, caused by the strong adsorption of St on this oxide phase. On α-$Fe_2O_3(0001)$ the coverages are lower and only 43% of all sites are blocked by St. This result is in line with the catalytic activities observed in the high pressure batch reactor experiments. $Fe_3O_4(111)$ is not active because of the styrene site blocking, α-$Fe_2O_3(0001)$ is active where atomic surface defects were identified as catalytically active sites. Thus, the surface chemical properties of the model catalyst films seem not to change significantly across the pressure-gap, and a new reaction mechanism for the ethylbenzene dehydrogenation over unpromoted α-Fe_2O_3 catalysts can be deduced, based on the surface science experimental results [37].
The size of the active defect sites is small compared to the size of the EB molecule, which makes it plausible that the ensemble of atoms forming an active site consists of the defect plus some flat terrace surface in the proximity of this defect. In contrast to all previously proposed mechanisms EB does not adsorb via the ethylgroup but via the phenyl ring. It adsorbs onto regular terrace sites with the phenyl ring oriented parallel to the surface as depicted in Fig. 8. The interaction of the π-electron system with acidic Fe^{3+} sites polarizes the molecule which may activate the C-H bonds in the ethyl group. Since the ethyl group, which must react, is bent relative to the aromatic plane by about 70°, steps or defects provide deviations from the flat geometry that allow intimate contact of the ethyl group with the catalyst. At a step, which is the dominant type of defect observed with STM, Brønsted basic oxygen sites deprotonate two C-H groups of the ethyl group, and a transition state with a fully conjugated conducting π-electron system is formed. We propose the transfer of the two electrons to occur via this π-electron system to two Fe^{3+} surface sites located underneath the phenyl ring. This combined acid-base redox reaction results in adsorbed styrene and an intermediate catalyst state with two surface hydroxyl groups and two reduced Fe^{2+} species.

$$2Fe^{3+}O^{2-} + EB_{ad} \rightarrow 2\,Fe^{2+}OH^- + St_{ad} \quad (5)$$

The catalytic cycle gets formally completed by desorption of St and hydrogen and reoxidation of Fe^{2+} to Fe^{3+}:

$$2Fe^{2+}OH^- + St_{ad} \rightarrow 2Fe^{3+}O^{2-} + St + H_2 \quad (6)$$

One might also consider a dehydrogenation of the molecule without electron transfer and formation of OH groups on the catalyst surface, which has to be clarified in future experiments with isotope labeled ethylbenzene. In any case, while the deprotonation or dehydrogenation takes place at defect sites, the adsorption-desorption kinetics is controlled by coupling between the reactant phenyl rings and the regular catalyst surface. This picture agrees with the structure reactivity correlations observed across the pressure gap on the model catalyst films. Surface defects on α-$Fe_2O_3(0001)$ increase the number of active sites but do not change the adsorption-desorption kinetics, which seems to control the catalyst activity for a given number of defects. It is unlikely that the different activities of Fe_3O_4 and α-Fe_2O_3 are caused by different basicities of their oxygen sites. Like for the heterolytic dissociation of water on $Fe_3O_4(111)$, a favorable geometric arrangement of pairs of acidic and basic sites on the catalyst surface is crucial, which must fit to the geometry of the educt molecule.
These findings agree with kinetic measurements performed over polycrystalline unpromoted and potassium-promoted iron oxide catalyst samples. There, the reaction rate was also found to depend on the reactant adsorption-desorption equilibria

with a site blocking effect caused by stronger adsorbed styrene [43]. Since similar apparent activaton energies on unpromoted and potassium promoted catalysts indicate the existence of active sites with similar properties, the mechanism found on the model catalyst films may also descibe the function of technical catalysts under high pressure conditions. We propose that on technical catalysts the active defect sites are generated in the reactant atmosphere during the activation period, which lasts about 20 hours during which a gradual increase of the catalayst activity is observed. On the model catalyst films the active defect sites must exist already before the batch reactor experiment, because hydrocarbon layers are formed which deactivate the films after about 50 min and therefore prevent steady state measurements over longer times where more defects might form. The hydrocarbon formation increases with the catalytic film activities, and most likely polystyrene is formed due to the long contact times in the batch reactor, a problem well known from technical catalysts [40]. The carbonaceous deposits start to nucleate at different regions on the catalyst surfaces and continue to grow forming patches on the surface. Such a nucleation and growth mechanism for carbonaceous surface deposits has been proposed previously [52]. It can explain the slower deactivation by coke of fresh prepared technical catalysts without nucleation centers if compared to catalysts regenerated by steam with nucleation centers left on the surface, since the nucleation process on fresh catalysts takes more time than the growth on regenerated catalysts with nuclei already present.

Although the catalytic activities of polycrystalline catalysts and of the model systems studied here are clearly correlated to the styrene adsorption energy, the styrene product desorption seems not to be the rate-determining step because the activation energy for this process on α-Fe_2O_3(0001) is considerably smaller (67 kJ/mol) than apparent activation energies reported for polycrystalline Fe_2O_3 catalysts (150-170 kJ/mol [36, 41, 44, 91]). It is possible that the deprotonation of EB on the catalyst surface is the rate determining step with a larger activation energy, another possibility is the involvement of water in the reaction mechanism. Instead of H_2 desorption from the two hydroxyl groups formed on the catalyst surface after the EB deprotonation, H_2O containing a lattice oxygen atom may desorb thereby reducing the catalyst surface:

$$2Fe^{2+}OH^- + St_{ad} \rightarrow Fe_2^{3+}O^{2-} + St + H_2O \qquad (7)$$

The catalyst surface is reoxidized by homolytically dissociated water:

$$H_2O + Fe_2^{3+}O^{2-} \rightarrow 2Fe^{3+}O^{2-} + H_2 \qquad (8)$$

This would result in an oxo-dehydrogenation mechanism with water as an oxidant. A homolytic dissociation of water might occur at the high reaction temperature of 900 K, since a heterolytic dissociation occurs already at room temperature. A further scenario is the formation of catalytically “active coke” on the catalyst surface under reaction conditions, resulting in a co-catalytic process. A catalytic formation of styrene by hydrocarbon overlayers was observed on several oxide substrates in the presence of oxygen gas [51, 92, 93]. The active coke consists of an organic polymer with quinone-like groups that contain oxygen atoms, which dehydrogenate the EB forming water as a product. Since no oxygen is present in the reactor atmosphere, such an oxo-dehydrogenation mechanism also requires the oxygen species to be provided from water, which must be split homolytically after being adsorbed dissociatively on the catalyst surface. These different scenarions have to be clarified in future studies.

The surface science experiments performed on single crystalline model systems under ultrahigh vacuum conditions clearly are correlated to the catalytic activities of these samples observed at high gas pressures, and correlations between the model systems and technical catalysts operating under real conditions were obtained as well. This demonstrates that the function of complex metal oxide catalysts can be elucidated by a fundamental surface science approach, if suitable model systems allowing high pressure reactivity studies are available. For determining the apparent activation energies of the styrene formation on the model catalyst films under even more realistic conditions a flow reactor system has been designed recently. Due to shorter contact times it allows to establish steady state conditions without deactivation of the model catalyst films by carbonaceous deposits, and first results on unpromoted and potassium promoted iron oxide model catalyst films were obtained recently [94]. These flow reactor mesurements will be simulated by state of the art microkinetic modeling, using adsorption-desorption kinetic parameters determined by TDS and UPS and considering gas flow patterns and temperature gradients inside the single crystal reactor. This allows to bridge the pressure-gap beyond the simple Langmuir model. The same modelling will be performed for kinetic measurements on polycrystalline catalyst samples in order to bridge the material gap. In this case the catalytic function of oxide materials could be understood on a fundamental level provided by surface science studies.

Acknowledgements

The authors gratefully acknowledge the excellent contributions of the following coworkers: Michael Ritter, Detlef Zscherpel, Wolfgang Ranke, Yvonne Joseph, Shamil Shaikhutdinov, Christian Kuhrs, Herbert Over, Sebastien Ragot, and Manfred Swoboda. Fruitful collaborations with Christoph Wöll, Mario Wühn, Thomas Schedel-Niedrig, and Axel Knop-Gericke are acknowledged. This project is funded in part by the Deutsche Forschungs-gemeinschaft.

References:

[1] G.A. Somorjai; in Introduction to Surface Chemistry and Catalysis, John Wiley & Sons, Inc. (1994).
[2] B. Hammer, Y. Morikawa, and J.K. Norskov; Phys. Rev. Lett. 76, (1996) 2141.
[3] A. Ruban, B. Hammer, P. Stoltze, H.L. Skriver and J.K. Norskov; J. of Molec. Catalysis A115 (1997) 421.
[4] J.A. Rodriguez and D.W. Goodman, Science 257 (1992) 897.
[5] M. Ruff, S. Frey, B. Gleich, and R.J. Behm; Appl. Phys. A66, (1998) 513.
[6] R.J. Behm; Acta Physica Polonica A, Vol. 93 (1998) 259.
[7] J.A. Rodriguez and W.A. Goodman, Surf. Sci. Rep. 14 (1991) 1.
[8] D.W. Goodman, R.D. Kelly, T.E. Madey, J.T. Yates; J. Catal. 63 (1980) 226.
[9] R.D. Kelley and D.W. Goodman; Surf. Sci. 123 (1982) L743.

[10] G. Ertl; in Catalytic Ammonia Synthesis, Ed. J.R. Jennings, Plenum, New York, 1983.
[11] P. Stoltze and J.K. Norskov; Phys. Rev. Lett. 55 (1985) 2502.
[12] R. Schlögl, R.C. Schoonmaker, M. Muhler and G. Ertl; Cat. Lett. 1 (1988) 237.
[13] M. Muhler, F. Rosowski and G. Ertl; Cat. Lett. 24 (1994) 317.
[14] R. Schlögl; in Handbook of Heterogeneous Catalysis, (Ed.: G. Ertl, H. Knözinger, J. Weitkamp), Wiley-VCH, Vol. 4, (1997) 1697.
[15] C.R. Henry, Surf. Sci. Rep. 31 (1998) 235.
[16] J.A. Jensen, K.B. Rider, M. Salmeron and G.A. Somorjai, Phys. Rev. Lett. 80 (1998) 1228.
[17] P.B. Rasmussen, B.L.M. Hendriksen, H. Zeijlemaker, H.G. Ficke and J.W.M. Frenken , Rev. Sci. Instrum. 69 (1998) 3879 .
[18] P.S. Cremer, X. Su, Y.R. Shen, and G.A. Somorjai, J. Mol. Cat. 131 (1998) 225.
[19] J.M. Thomas and W.J. Thomas, , Principles and Practice of Heterogeneous Catalysis, VCH Weinheim, Kapitel 1, 1997.
[20] S.L.M. Schroeder, G.D. Moggridge, T. Rayment and R.M. Lambert, J. Mol. Cat. A: Chemical 119 (1997) 357.
[21] M. Hävecker, A. Knop-Gericke and Th. Schedel-Niedrig, Appl. Surf. Sci. 142 (1999) 438.
[22] H.-J. Freund and E. Umbach, Eds., Adsorption on Ordered Surfaces of Ionic Solids and Thin Films, Vol.33 of Springer Series in Surface Science (Springer, Berlin, 1993).
[23] V.E. Henrich and P.A. Cox, The Surface Science of Metal Oxides (Cambridge Univ. Press, Cambridge, 1994).
[24] C. Noguera; Physics and Chemistry at Oxide Surfaces, Cambridge University Press 1996.
[25] D. Schmalzried; Chemical Kinetics of Solids, VCH, Weinheim, 1995.
[26] H.-J. Freund; Angewandte Chemie 109/5 (1997) 444.
[27] A. Stierle, Th. Knoll, and H. Zabel, Phys. Rev. B58 (1998) 5062.
[28] R.M. Jaeger, H. Kuhlenbeck, H.-J. Freund, M. Wuttig, W. Hoffmann, R. Franchy and H. Ibach; Surface Science 259 (1991) 235.
[29] V. Maurice, M. Salmeron and G.A. Somorjai; Surface Science 237 (1990) 116.
[30] K.-D. Schierbaum; Surface Science 399 (1998) 29.
[31] Th. Bertrams and H. Neddermeyer; J. Vac. Sci. Technol. B14 (1996) 1141.
[32] A.B. Boffa, H.C. Galloway, P.W. Jacobs, J.J. Benitez, J.D. Batteas, M. Salmeron, A.T. Bell and G.A. Somorjai; Surface Science 326 (1995) 80.
[33] L. Zhang, M. Kuhn and U. Diebold; Surface Science 375 (1997) 1.
[34] J. Wollschläger, D. Erdös, and K.-M. Schröder, Surf. Sci. 402 (1998) 272.
[35] S.C. Street, C. Xu and D.W. Goodman; Annu. Rev. Phys. Chem. 48 (1997) 43.
[36] K. Coulter, D.W. Goodman, R.G. More; Catal. Lett. 31 (1995) 1.
[37] W. Weiss, C. Kuhrs, Y. Josepf, W. Ranke, M. Wühn, and Ch. Wöll, submitted to Cat. Lett.
[38] H. Ohlinger and S. Stadelmann; in: Ullmanns Enzyklopädie der technische Chemie, Urban und Schwarzenberg, Vol. 16, 460, München-Berlin 1965.
[39] E.H. Lee; Calal. Rev. 8 (1973) 285.
[40] K. Kochloefl; in Handbook of Heterogeneous Catalysis, (Ed.: G. Ertl, H. Knözinger, J. Weitkamp), Wiley-VCH, Vol. 5 (1997) 2151.
[41] S. Carra and L. Forni; Ind. Eng. Chem. Process Des. Dev. 4 (1965) 281.
[42] N.N. Lebedev, G.V. Odabashyan, V.V. Lebedev, and M.G. Markov; Kinet. Katal. 18, (1977) 1177.
[43] T. Hirano; Appl. Catal. 26 (1986) 65.
[44] T. Hirano; Appl. Catal. 28 (1986) 119.
[45] W.P. Addiego, C.A. Estrada, D.W. Goodman, M.P. Rosynek, R.G. Windham; J. Catal. 146 (1994) 407.
[46] W.D. Mross; Catal. Rev. Sci. Eng. 25, (1983) 591.
[47] M. Muhler, J. Schütze, M. Wesemann, T. Rayment, A. Dent, R. Schlögl and G. Ertl; Journal of Catal. 126 (1990) 339.
[48] M Muhler, R. Schlögl and G. Ertl; J. Calal. 138 (1992) 413.
[49] M. Muhler; PhD thesis, Fritz-Haber-Institut, 1989.
[50] I. Wang, J.-C. Wu and C.-S. Chung; Appl. Catal. 16 (1985) 89.
[51] G. Emig and H. Hofmann; J. Catal. 84 (1983) 15.
[52] J. Choi and G. Eigenberger, Chem. Ing. Tech. 61 (1989) 641.
[53] G. Kolios and G. Eigenberger , Chem Eng. Sci. 54 (1999) 2637.
[54] W. Weiss, M. Ritter, D. Zscherpel, M. Swoboda and R. Schlögl; J. Vac. Sci. & Technol. A16 (1998) 21.
[55] W., Ranke and W. Weiss, Surf. Sci. 414 (1998) 238.
[56] M. Wühn, P.S. Bagus, S. Reiß, A. Niklewski, Y. Joseph, W. Weiss, R. Püttner, M. Martins, G. Kaindl, Ch. Wöll, submitted to J. Phys. Chem.
[57] A. Muan; Am. J. of Science 256 (1958) 171.
[58] G.H. Vurens, M. Salmeron and G.A. Somorjai; Surface Science 201 (1988) 129.
[59] H.C. Galloway, P. Sautet and M. Salmeron; Phys. Rev. B 54 (1996) R11145.
[60] Y.J. Kim, C. Westphal, R.X. Ynzunza, H.C. Galloway, M. Salmeron, M.A. Van Hove and C.S. Fadley ; Phys. Rev. B55 (1997) R13448.
[61] M. Ritter, W. Ranke and W. Weiss; Phys. Rev. B57 (1998) 7240.
[62] W. Ranke, M. Ritter and W. Weiss, Phys. Rev. B60 (1999) 1527.
[63] W. Weiss and M. Ritter, Phys. Rev. B59 (1999) 5201.
[64] Sh.K. Shaikhutdinov, M. Ritter, X.-G. Wang, H. Over, W. Weiss, Phys. Rev. B60 (1999) 11062.
[65] R.W.G. Wyckoff; Crystal Structures, 2nd ed., Vol. II, p.167, Interscience Publishers (1982).
[66] M. Ritter and W. Weiss; Surf. Sci. 432 (1999) 81.
[67] R.W.G. Wyckoff, Crystal Structures, Interscience Publishers, 2nd ed., 1982, Vol. II, p.1.

[68] X.-G. Wang, W. Weiss, Sh.K. Shaikhutdinov, M. Ritter, M. Petersen, F. Wagner, R. Schlögl and M. Scheffler; Phys. Rev. Lett. 81 (1998) 1038.
[69] Sh. K. Shaikhudtinov and W. Weiss, Surf. Sci. 432 (1999) L627.
[70] G. Ketteler and W. Weiss, in preparation.
[71] Th. Schedel-Niedrig, W. Weiss and R. Schlögl; Phys. Rev. B 52 (1995) 17449.
[72] W. Weiss; Surface Science 377 (1997) 943.
[73] Y.Q. Cai, M. Ritter, W. Weiss and A.M. Bradshaw; Phys.Rev.B, in press.
[74] R.M. Cornell and U. Schwertmann; The Iron Oxides, VCH Weinheim 1996.
[75] Z. Zhang and S. Satpathy; Phys. Rev. B44 (1991) 13319.
[76] W.C. Mackrodt, F. Jollet, and M. Gauthier-Soyer, Phil. Mag. B79 (1999) 25.
[77] A. Fujimori, M. Saeki, N. Kimizuka, M. Taniguchi, and S. Suga; Phys. Rev. B34 (1986) 7318.
[78] R.J. Lad and V.E. Henrich; Phys. Rev. B39 (1989) 13478.
[79] D.W. Turner, A.D. Baker, C. Baker, and C.R. Brundle; Molecular Photoelectron Spectroscopy (Wiley-Interscience, New York 1970).
[80] Y. Joseph, W. Ranke, W. Weiss, J. Phys. Chem. 1999, in press.
[81] Y. Joseph, C. Kuhrs, W. Ranke, M. Ritter, W. Weiss, Chem. Phys. Lett. (1999) in press.
[82] P.A. Thiel and T.E. Madey; Surf. Sci. Rep. 7 (1987) 211.
[83] Sh.K. Shaikhutdinov and W. Weiss, J. Mol. Cat. 1999, in press.
[84] D. Zscherpel, W. Ranke, W. Weiss, and R. Schlögl, J. Chem. Phys. 108 (1998) 9506.
[85] Sh.K. Shaikhutdinov, W. Ranke, Y. Joseph, C. Kuhrs, W. Weiss, Faraday Discussion 114 (1999) in press.
[86] J. K. Norskov and P. Stoltze; in: Handbook of Heterogeneous Catalysis, Vol. 3, p. 983 (Eds.: G. Ertl, H. Knözinger, J. Weitkamp), Wiley-VCH 1997.
[87] K. Christmann; Surface Physical Chemistry, Steinkopff, Darmstadt 1991.
[88] W. Weiss, D. Zscherpel and R. Schlögl, Catal. Lett. 52 (1998) 215.
[89] M. Henzler ; in: Electron Spectroscopy for Surface Analysis, ed. by H. Ibach, Springer, Berlin, 1979.
[90] W. Weiss, D. Schmeisser and W. Göpel; Surface Science 207 (1989) 401.
[91] P. Tetenyi, Z. Paal, M. Dobrovolszk; Z. Phys. Chemie 102 (1976) 267.
[92] G.C. Grunewald and R.S. Drago; J. of Molecul. Catal. 58 (1990) 227.
[93] A. Guerrero-Ruiz and I. Rodriguez-Ramos; Carbon 32 (1994) 23.
[94] C. Kuhrs and W. Weiss, submitted to Int. Catal. Conf. Proc., Granada 2000.

Figures:

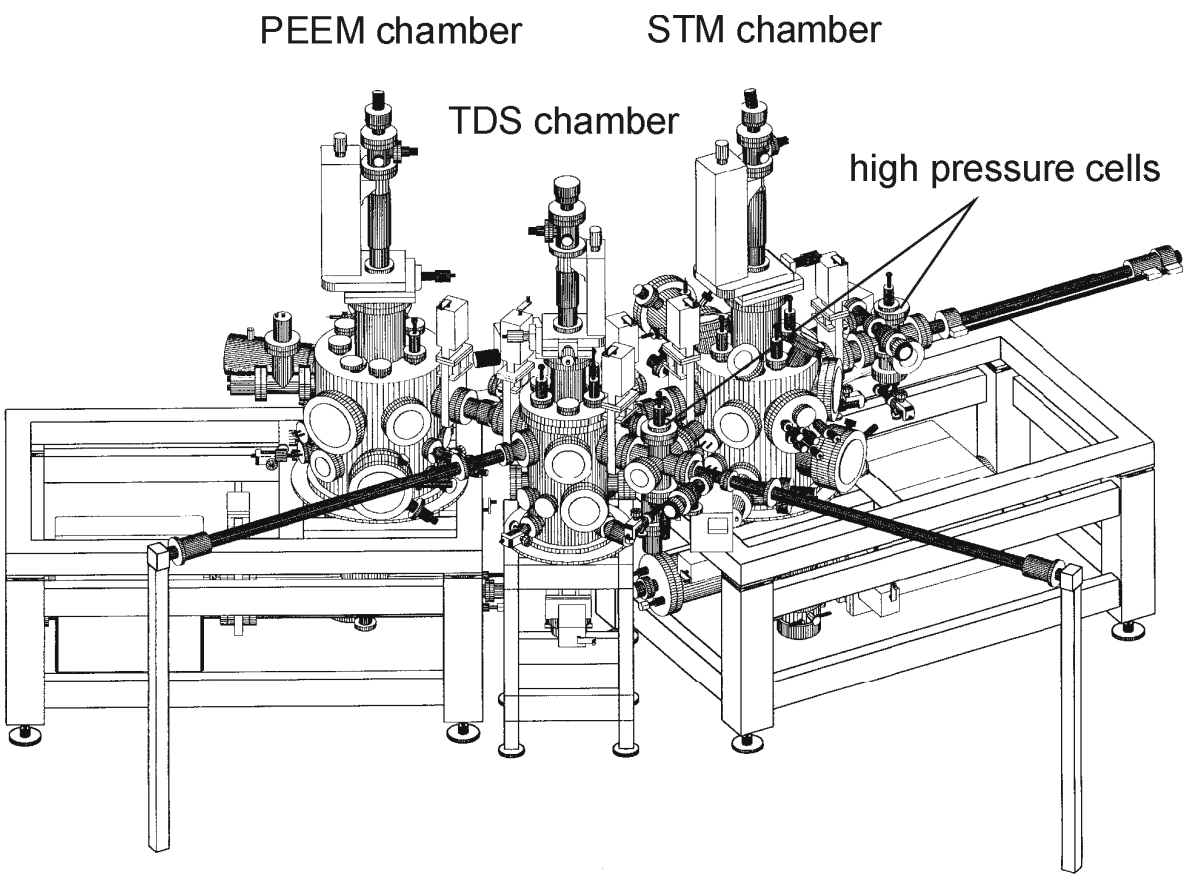

Fig. 1: Perspective side view of the three chamber surface analysis system combined with high pressure reaction cells.

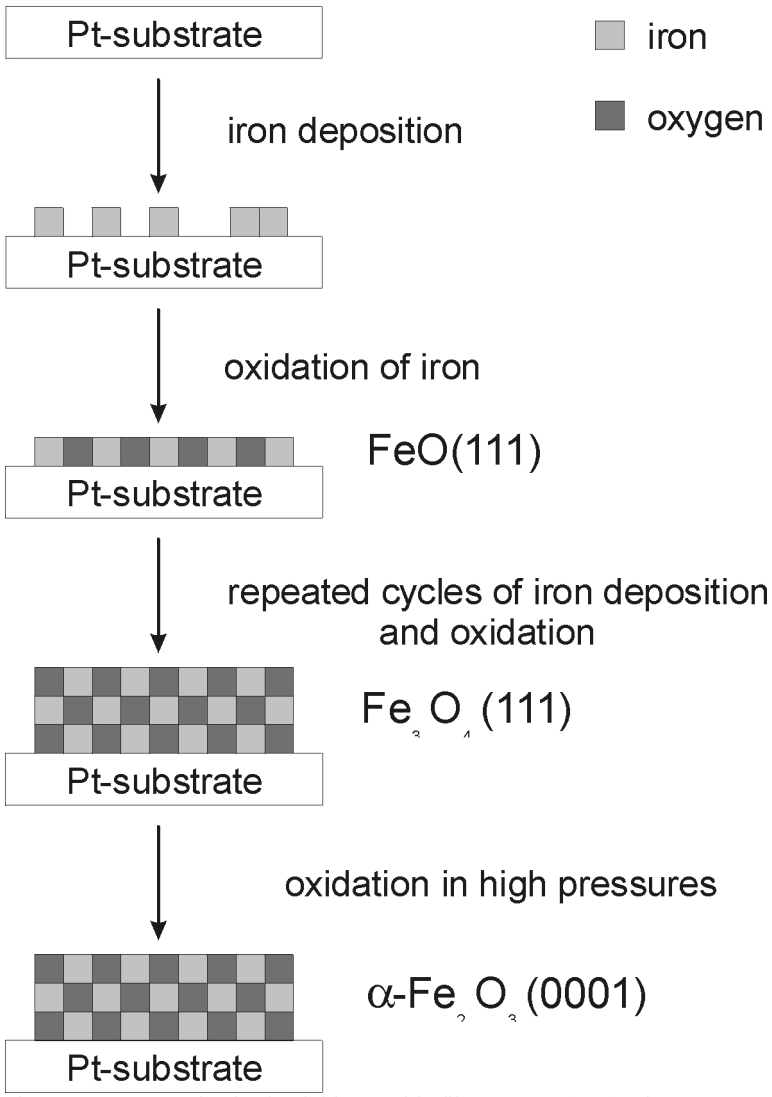

Fig. 2: Growth of epitaxial iron oxide films onto Pt(111) substrates, accomplished by repeated cycles of iron deposition and subsequent oxidation.

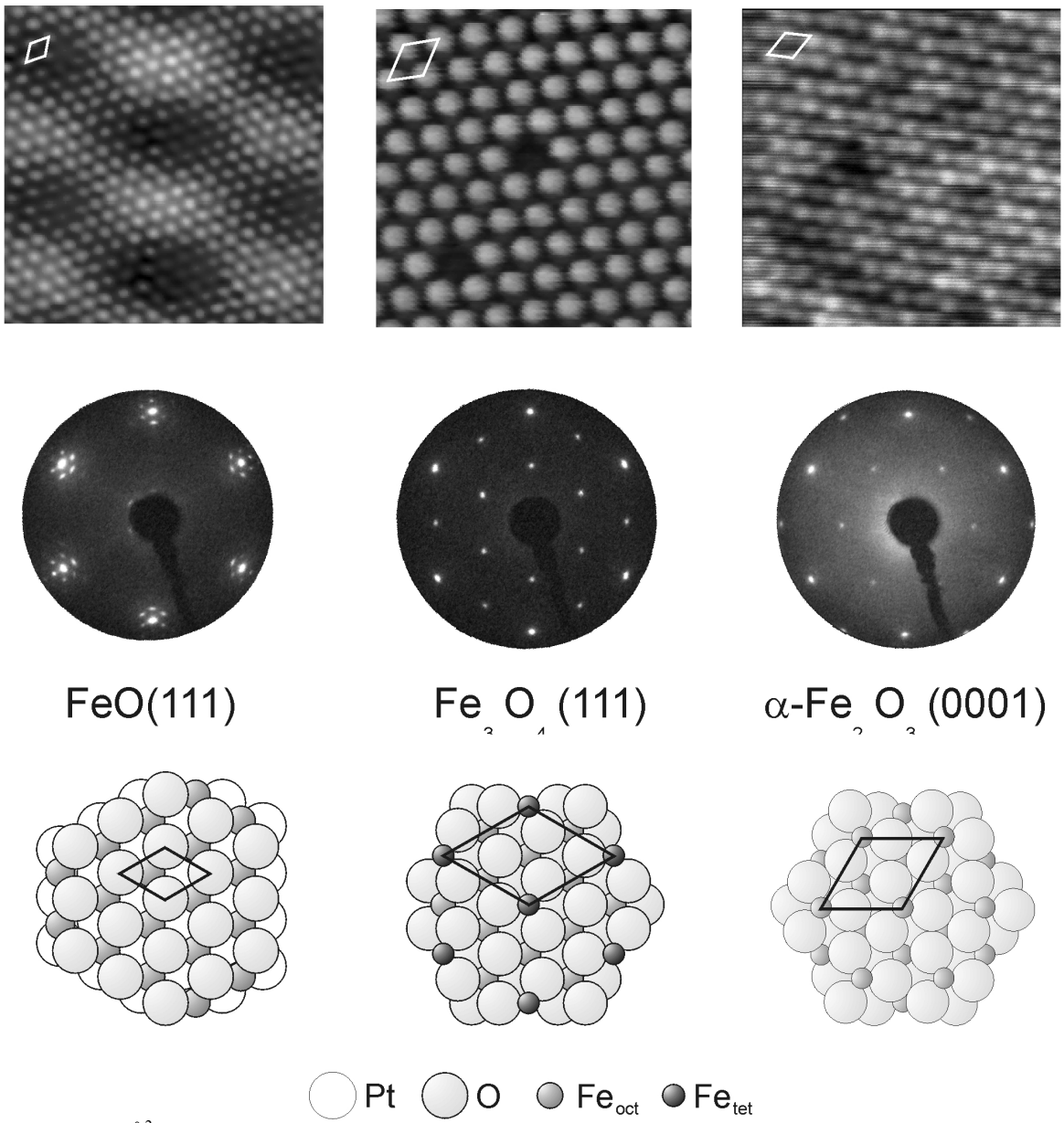

Fig.3: 55×55 Å^2 atomic resolution STM images (top), surface structure models in top view representation (middle), and LEED patterns taken at E=60 eV (bottom) of the three iron oxide films grown onto Pt(111). The surface unit cells are indicated.

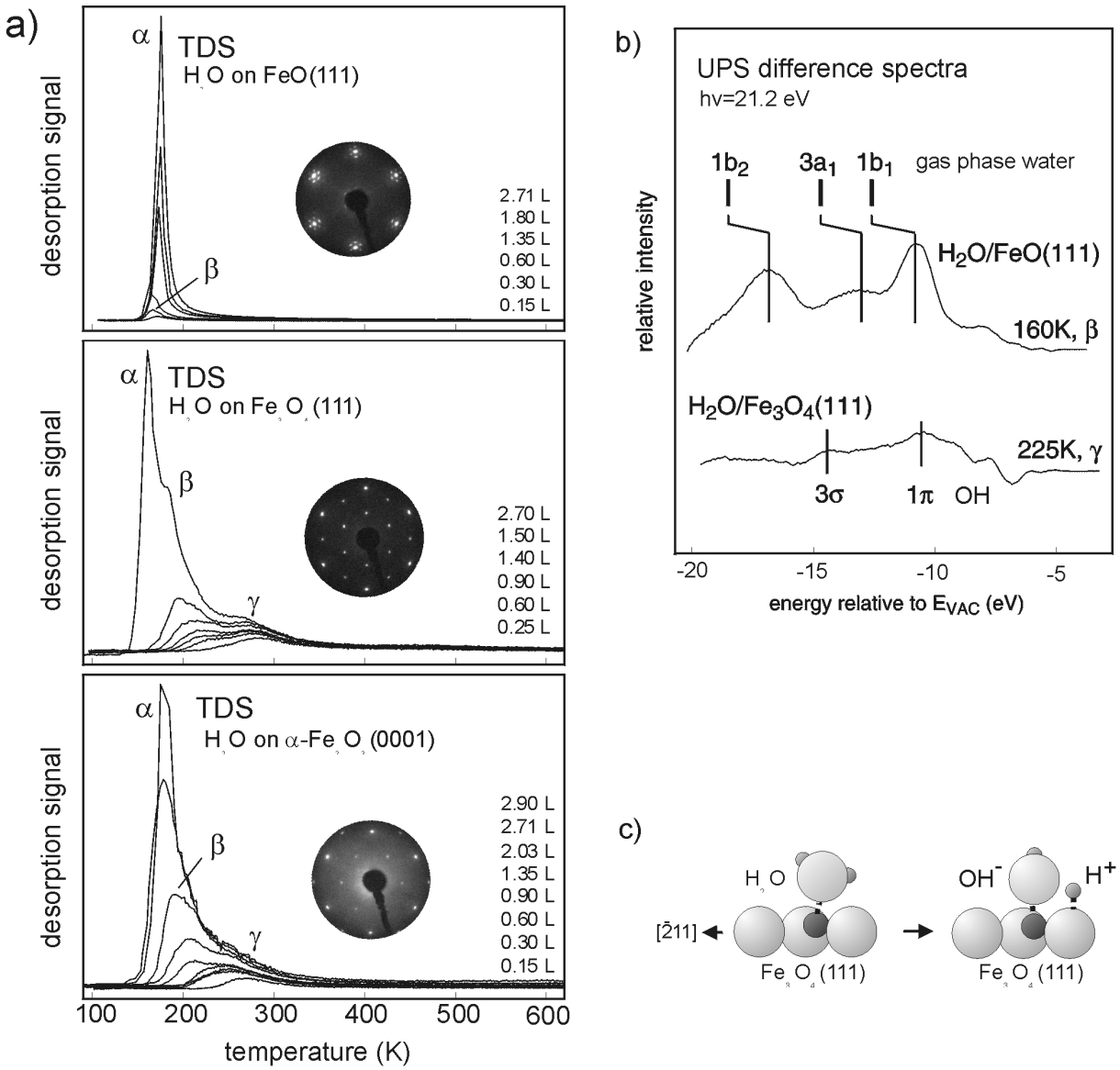

Fig. 4: a) Thermal desorption traces of water adsorbed on FeO(111), Fe_3O_4(111) and α-Fe_2O_3(0001) at T=100 K. Exposures are indicated in Langmuir units. The inserts show LEED patterns of the clean oxide films.

b) UP valence band spectra difference spectra measured under adsorption-desorption equilibrium conditions at a constant water vapor pressure of 10^{-8} mbar and the indicated temperatures. On FeO(111) monomeric water is physisorbed, on Fe_3O_4(111) hydroxyl species are formed due to dissociation of water.

c) Schematic side view representation of a water molecule associatively adsorbed via its oxygen atom onto an Fe cation on Fe_3O_4(111). After the heterolytic dissociation OH^- and H^+ species are bound to Lewis acidic Fe and Brønsted basic O sites, respectively. The strongly relaxed Fe_3O_4(111) surface structure was detemined by LEED crystallography [66].

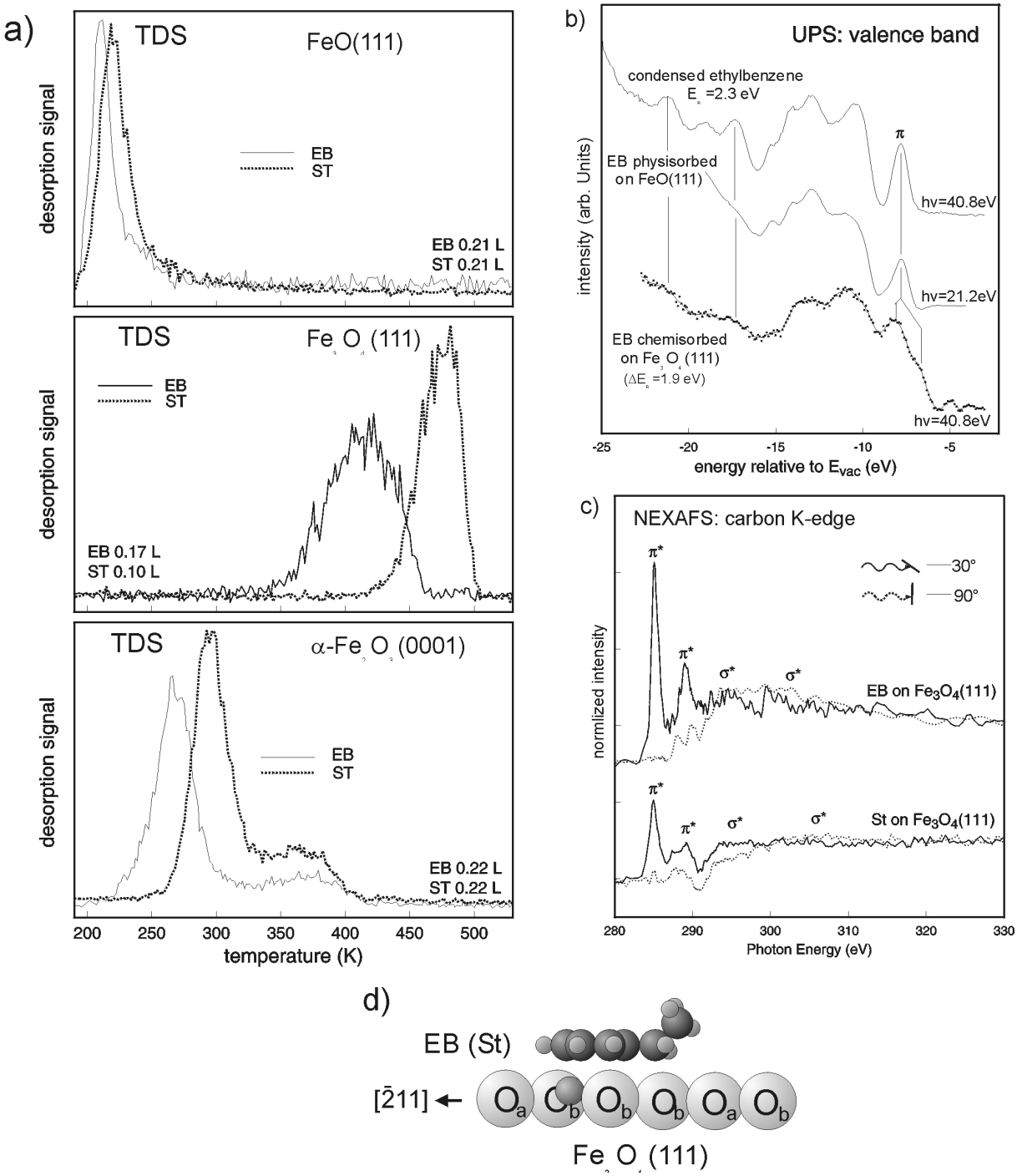

Fig. 5 a) Thermal desorption traces of the most strongly bound ethylbenzene (EB) and styrene (St) species on FeO(111), Fe_3O_4(111) and α-Fe_2O_3(0001), measured after small exposures at T=100 K given in Langmuir units. The inserts show LEED patterns of the clean oxide films.

b) UP valence band difference spectra of a condensed ethylbenzene multilayer, ethylbenzene physisorbed on oxygen terminated FeO(111) and chemisorbed on iron terminated Fe_3O_4(111). The latter has been shifted to adjust the low lying levels with those of condensed ethylbenzene. The comparison shows that EB chemisorbs via a specific interaction of the phenyl ring π-electron system with acidic surface iron atoms. A similar behavior is observed for styrene.

c) NEXAFS spectra of EB and St chemisorbed on Fe_3O_4(111), measured at two different angles of incidence. Similar spectra are observed on α-Fe_2O_3(111).

d) Orientation of ethylbenzene chemisorbed on Fe_3O_4(111) with the phenyl ring parallel to the surface. The same adsorption geometries were found styrene on Fe_3O_4(111) as well as for ethylbenzene and styrene on α-Fe_2O_3(0001). The two surface structures were detemined by LEED crystallography [66, 70].

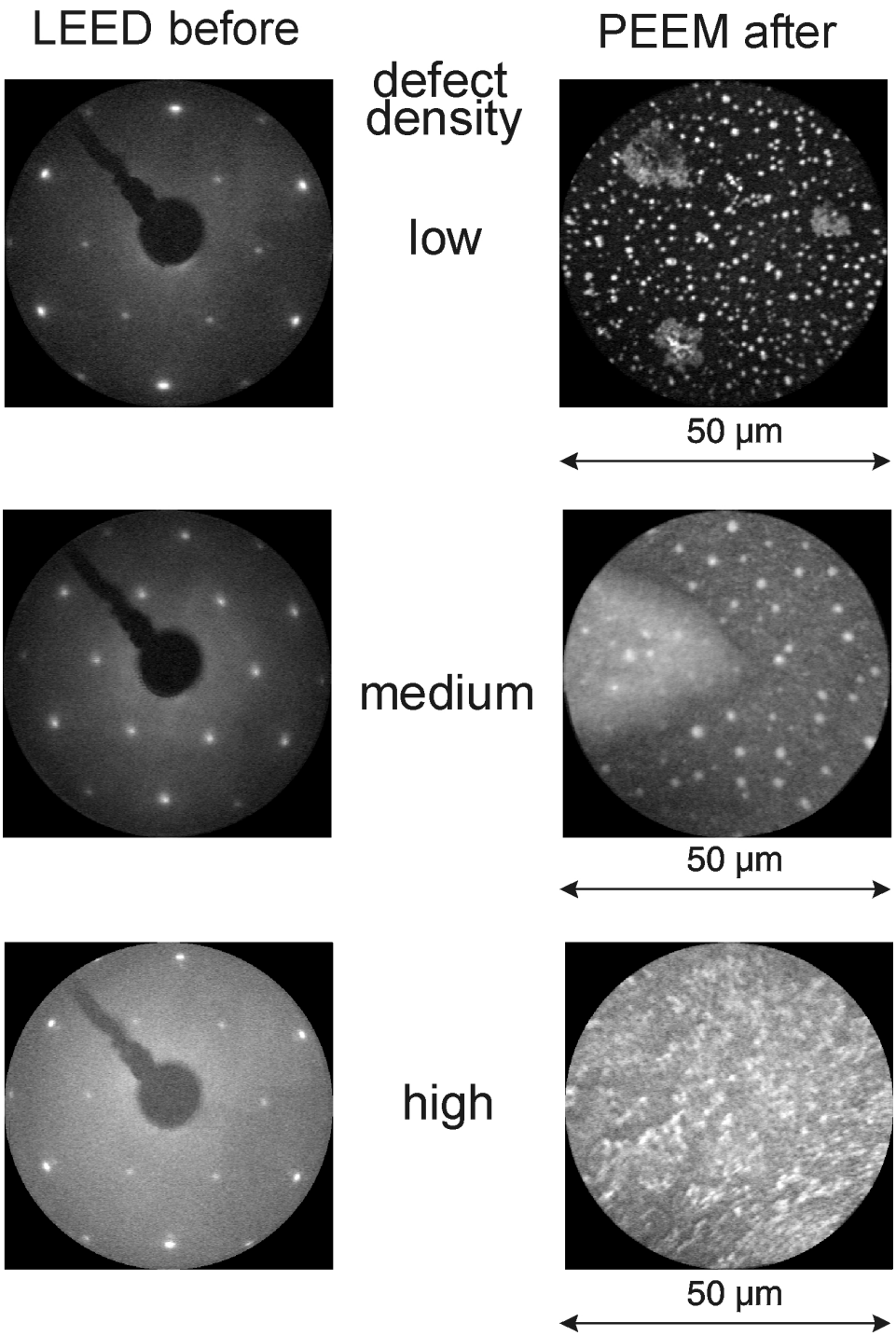

Fig. 6: On the left-hand side the LEED patterns of Fe_2O_3(0001) films taken at E=60 eV before the batch reactor experiments are shown. The surface defect concentrations are indicated, which were deduced from the diffuse background intensities and diffraction spot profiles in the LEED patterns. On the right-hand side 50 µm diameter PEEM images observed on the three films after the reaction experiments are shown, where carbonaceous surface deposits are visible as bright patches.

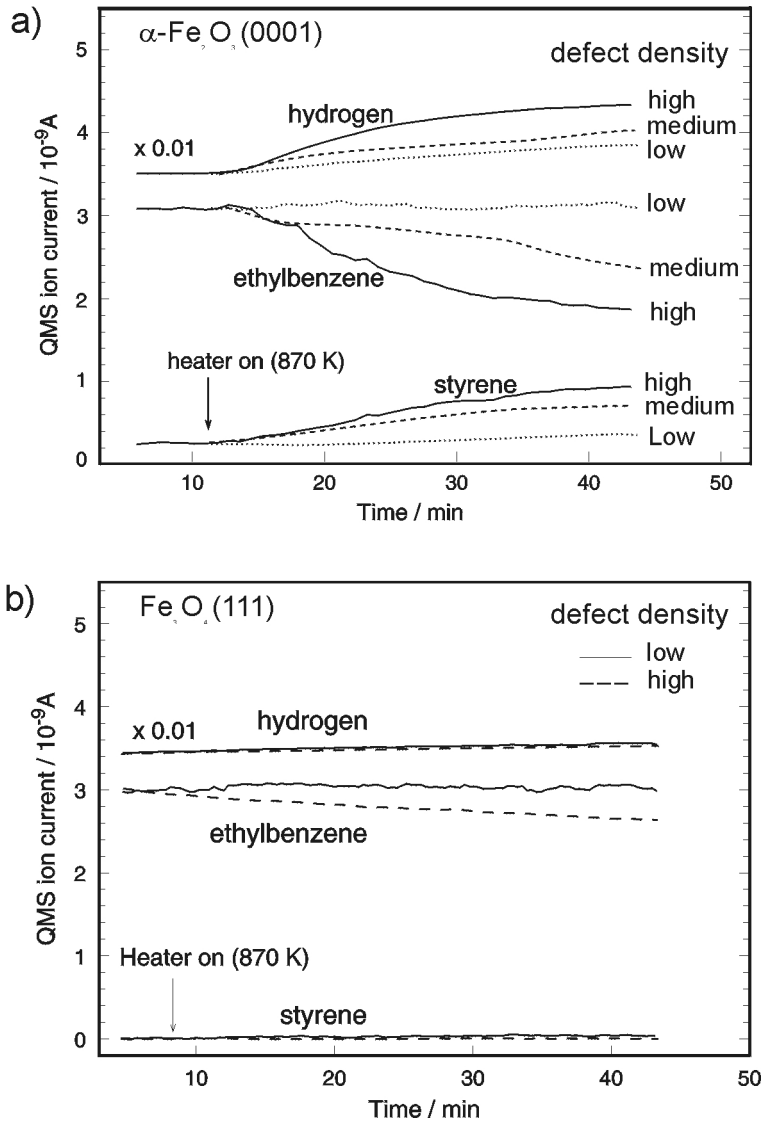

Fig. 7 a) Batch reactor experiments on epitaxial Fe_2O_3(0001) films with different surface defect concentrations. A mixture of ethylbenzene and water with a molar ratio of 1:10 and a total pressure of 0.6 mbar was established in the reactor. The concentrations of hydrogen, EB and styrene in the reactor are displayed as a function of time. An offset was added to the hydrogen signal for better presentation.

b) Batch reactor experiments on epitaxial Fe_3O_4(111) films with low and high surface defect concentrations under the same conditions as in b).

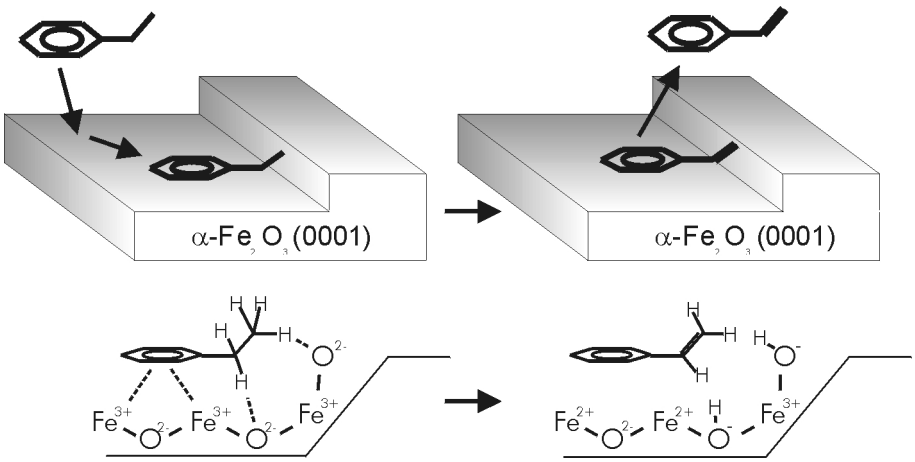

Fig. 8: Mechanism proposed for the styrene synthesis reaction on α-Fe_2O_3(0001) model catalyst films. Ethylbenzene adsorbs at Fe^{3+} sites exposed on regular terraces with the phenylring oriented parallel to the surface. At catalytically active surface defects like steps the upward tilted elthylgroup meets a favorable geometry for coupling to Brønsted basic oxygen sites that deprotonate two C-H groups, simultaneously two electrons are transferred to the catalyst via the π-electron system of the phenyl ring.